THE JOURNAL OF PHYSICAL CHEMISTRY B

pubs.acs.org/JPCB Article

Direct Measurement of Single-Molecule Ligand−Receptor Interactions

K.-T. Lam, E. L. Taylor, A. J. Thompson, M.-D. Ruepp, M. Lochner, Michael J. Martinez, and J. A. Brozik*

Cite This: J. Phys. Chem. B 2020, 124, 7791−7802

Read Online

ACCESS | Metrics & More | Article Recommendations

ABSTRACT: Measuring the kinetics that govern ligand−receptor interactions is fundamental to our understanding of pharmacology. For ligand-gated ion channels, binding of an agonist triggers allosteric motions that open an integral ion-permeable pore. By mathematically modeling stochastic electrophysiological responses with high temporal resolution (ms), previous single channel studies have been able to infer the rate constants of ligands binding to these receptors. However, there are no reports of the direct measurement of the single-molecule binding events that are vital to how agonists exert their functional effects. For the first time, we report these direct measurements, the rate constants, and corresponding free energy changes, which describe the transitions between the different binding states. To achieve this, we use the super resolution technique: points accumulation for imaging in nanoscale topography (PAINT) to observe binding of ATP to orthosteric binding sites on the P2X1 receptor. Furthermore, an analysis of time-resolved single-molecule interactions is used to measure elementary rate constants and thermodynamic forces that drive the allosteric motions. These single-molecule measurements unequivocally establish the location of each binding states of the P2X1 receptor and the stochastic nature of the interaction with its native ligand. The analysis leads to the measurement of the forward and reverse rates from a weak ligand-binding state to a strong ligand binding state that is linked to allosteric motion and ion pore formation. These rates (k_α = 1.41 sec^{-1} and k_β = 0.32 sec^{-1}) were then used to determine the free energy associated with this critical mechanistic step (3.7 kJ/mol). Importantly, the described methods can be readily applied to all ligand-gated ion channels, and more broadly to the molecular interactions of other classes of membrane proteins.

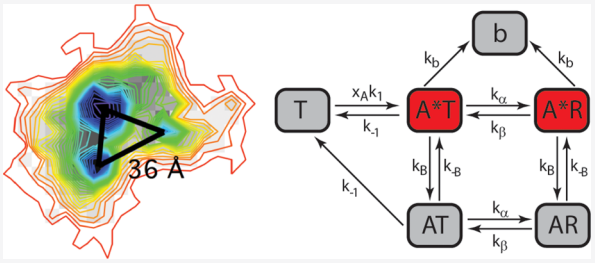

1. INTRODUCTION

Understanding how ligands bind to their receptors is of fundamental importance in pharmacological research, enabling researchers to understand the underlying dynamics of an interaction and to effectively develop novel therapeutics. Measurement of these interactions is often made using methods that yield ensemble averages such as radioligand binding or surface plasmon resonance.[1,2] Often, the averaged results of these methods do not reveal all of the possible states that can exist in the receptor−ligand system, as many of them remain hidden or obscured by ensemble average. For other methods such as X-ray crystallography and atomic force microscopy, the images are static and provide no means of measuring kinetics. Electrophysiology is one method that can observe the underlying kinetics of single molecules; however, even this method must infer binding states from the indirect measurement of channel gating.[3−5] A more widely applicable and direct method of monitoring ligand binding is the use of single-molecule fluorescence imaging, in which the binding of fluorescent ligands is monitored by time-lapse single-molecule fluorescence microscopy.[6−9] This results in discrete observations of individual receptors bound with one or more of their ligands, and the subsequent movies of these events can be analyzed to determine key components of the interactions and the associated particle-based kinetics that arise.

For kinetic studies, deterministic chemical kinetics is generally more applicable, but single particle-based kinetics is more fundamental and closer to reality, just as statistical mechanics is closer to reality when compared to continuum thermodynamics. A key advantage of these particle-based kinetic experiments is that individual rate constants can be estimated from the fluctuations of the system at equilibrium. This stems from the basic assumption used to derive the fluctuation−dissipation theorem, which states that the response of a system at thermodynamic equilibrium to a

Received: June 16, 2020
Revised: August 6, 2020
Published: August 11, 2020

https://dx.doi.org/10.1021/acs.jpcb.0c05474
J. Phys. Chem. B 2020, 124, 7791−7802

small force is the same as its response to a spontaneous fluctuation.[3] As such, particle-based kinetics treat the chemical components of a system as discrete variables that fluctuate from one chemical state to the next and places the classical rate equations that describe these transitions into a probabilistic framework.[10] Using this probabilistic framework, stochastic rate data can be expressed as a histogram and fit to a probability density function (PDF) derived from the solution of a stochastic rate equation. Alternatively, the stochastic rate data can be treated as a time-continuous stream of fluctuating chemical events following a Markovian chain based on the probability of the system making chemical transitions (experimentally, time is almost always discretized due to the collection times of the experiment). Data treated in this manner can be analyzed using a Hidden Markov Model (HMM) in which an observation is related to the state of the system. However, these observations are insufficient to precisely determine the state of the system and as a consequence, a maximum-likelihood algorithm, such as Baum−Welch, is used to estimate the transition probabilities between discrete states, giving rates and accompanying rate constants. Hidden Markov analysis (HM analysis) has been used to determine stochastic kinetic rate constants that give rise to single-channel currents since the 1970s.[4,5,11−15] More recently, these stochastic analyses have been employed in a number of single-molecule fluorescence studies.[16−19] These methods rely solely on the appearance or disappearance of signal from a single probe molecule, but the adoption of these techniques to determine single-molecule kinetics has lagged because of the difficulty arising from the fluctuational characteristics of individual probe molecules.

Herein, we provide the first description of time-lapse single-molecule fluorescence microscopy to study the binding of a fluorescently labeled ligand (ATP) to its native ion channel (the P2X1 receptor). We show the rate constants that govern transitions between weak and strong ligand binding states, and reveal a free-energy driving force weighted to the strong binding state that is about 1.5 times that of $N_A k_B T$.

2. MATERIALS AND METHODS

2.1. Materials. All lipids were purchased from Avanti Polar Lipids, Inc. (Alabaster, AL, USA). 2′/3′-O-(2-aminoethylcarbamoyl)-adenosine-5′-triphosphate, labeled with ATTO-700 (ATP*), was purchased from Jena Bioscience (Jena, Germany). All components for buffers were purchased from Sigma-Aldrich Co (St Louis, MO, USA). ATTO-700-DPPE (DPPE = 1,2-dipalmitoyl-*sn*-glycero-3- phosphoethanolamine) was purchased from ATTO-TEC GmbH (Siegen, Germany).

2.2. Plasmids. The lentiviral FLAG-tagged human P2X1 expression construct and the pLV-tTR-Krab-Blast plasmid used for the generation of the stable expression cell line are described in detail elsewhere.[20]

2.3. Cell Culture and Stable Cell Line Generation. HEK 293 T cells were cultured at 37 °C and 5% CO_2 in $DMEM^{+/+}$ (DMEM supplemented with 10% fetal calf serum and 1x Pen/Strep (100 IU/mL penicillin and 100 μg/mL streptomycin)). The generation of the inducible P2X1-FLAG-IRES-IFP1.4 cell line is described in detail elsewhere.[20] In brief, 80% confluent HEK 293 T cells were transfected with pLV-tTR-Krab Blast, pCMVR8.91, and pMD2.G[21] using FuGene HD according to the manufacturer's instructions. Lentiviral supernatants were harvested 2, 3, and 4 days post-transfection and cleared by filtration through a 0.45 μM polyethersulfone sterile filters (Millipore Corp, Burlington, MA, USA). To generate the stable HEK 293 T tTR-Krab Blast cell line, HEK 293 T cells were incubated with lentiviral supernatants supplemented with 5 μg mL^{-1} polybrene (hexadimethrine bromide, Sigma-Aldrich, St. Louis, MO, USA). To reduce polybrene toxicity, DMEM+/+ was added 7 hours post transduction to reduce the polybrene concentration to 2.5 μg mL^{-1}. After expansion and selection of the transduced cells with Blasticidin, a second round of virus production was started with pLV-P2X1-IRES.IFP1.4, pCMVR8.91, and pMD2.G. HEK 293 T tTR-Krab Blast cells were incubated with filtered pLV-P2X1-IRES.IFP1.4 lentiviral supernatants to generate the inducible P2X1-FLAG-IRES-IFP1.4 cell line. Cells with a high level of IFP1.4 expression were selected by fluorescence-activated cell sorting (FACS) after incubation of transduced cells with doxycycline and biliverdin for 48 h.

2.4. Protein Purification. P2X1-FLAG was purified essentially according to.[20] In brief, stable P2X1-FLAG cells were cultured in T300 flasks and incubated with doxycycline to induce expression 48 h before harvesting. The medium was removed, and cells were washed 1x with phosphate-buffered saline (PBS; 137 mM NaCl, 4.3 mM Na_2HPO_4, 2.7 mM KCl, 1.47 mM KH_2PO_4, pH 7.4) and detached by trituration with PBS. Harvested cells were pelleted for 5 min at 500 g followed by snap-freezing in liquid N_2. The cell pellets were then stored at −80 °C until further processing. For the purification, 2 mL Tris-EDTA (50 mM Tris−HCl, 0.5 mM EDTA, pH 7.5) supplemented with 1x Halt Protease Inhibitor (Pierce, Thermo Scientific, IL, USA), 2.5 mM $MnSO_4$, and 125 U/mL Cyanase (Ribo Solutions Inc.) were added to the cell pellet. The cell suspension was then homogenized using a 5 mL cell-douncer followed by trituration through 21-gauge and 27-gauge needles. The membrane fraction was collected by centrifugation for 30 min at 100,000 × *g* and resuspended in 10 mL solubilization buffer (100 mM NaCl, 0.54 mM KCl, 2 mM Na_2HPO_4, 0.4 mM KH_2PO_4, pH 7.4, and 2 mM $C_{12}E_9$), followed by a 1 h head over tail incubation at 4 °C. The solubilized membrane fraction was then subjected to centrifugation at 100,000 × *g* for 1 h. The recovered supernatant containing solubilized P2X1-FLAG was incubated with anti-FLAG M2 agarose beads (Sigma-Aldrich, St Louis, MO, USA) for 2 h head-over-tail at 4 °C. The beads were washed five times with wash buffer (100 mM NaCl, 0.54 mM KCl, 2 mM Na_2HPO_4, 0.4 mM KH_2PO_4, pH 7.4, and 0.4 mM $C_{12}E_9$) and immunoprecipitated receptors were eluted by incubating the beads 30 min head over tail in wash buffer supplemented with 1 mg mL^{-1} FLAG peptide (Pepnome Ltd., Zhuhai, China). The eluate was separated from the beads by centrifugation through Micro Bio-Spin columns (Bio-Rad, California, USA) at 500 × *g* for 1 min. The recovered eluate was dialyzed overnight in a 10 K MWCO Slide-A-Lyzer cassette (Pierce, Thermo Scientific, IL USA) against wash buffer. The next day, purified receptors were aliquoted followed by snap-freezing in liquid N_2 and stored at −80 °C. Purity and yield were assessed by SDS-Page on a 4−12% NuPAGE Novex Bis-Tris gel (Life Technologies, Carlsbad, CA, USA) followed by Imperial Protein Staining (Pierce, Thermo Fisher Scientific).

2.5. Vesicle Preparation. Three types of small unilamellar vesicles (SUVs) were prepared: (1) SUVs used in the P2X1 receptor experiments (P2X1-liposomes), (2) SUVs used in the characterization of the ATTO-700 probe molecule (DPPC-

https://dx.doi.org/10.1021/acs.jpcb.0c05474
J. Phys. Chem. B 2020, 124, 7791−7802

liposomes), and (3) SUVs for fluorescence recovery after photobleaching (FRAP) experiments (FRAP-liposomes). P2X1-liposomes were prepared from lipid cakes made by evaporating 1 mL of a 9:1 chloroform:methanol solution that contained 3.93 μmol 1,2-dimyristoyl-*sn*-glycero-3-phos-phocholine (DMPC), 0.07 μmol 1,2-dioleoyl-*sn*-glycero-3-phosphoethanolamine-*N*-[methoxy(poly-ethyleneglycol)-2000] (ammonium salt) (PEG-PE), and 1 μmol L-α-phosphatidyl-serine (Brain-PS). DPPC-liposomes were prepared from lipid cakes made by evaporating 1 mL of a 9:1 chloroform:methanol solution that contained 5 μmol 1,2-dipalmitoyl-*sn*-glycero-3-phosphocholine (DPPC). FRAP-liposomes were the same as the P2X1-liposomes except the lipid cake also contained 0.005 μmol 1,2-dimyristoyl-*sn*-glycero-3-phosphoethanolamine-*N*-(lissamine rhodamine B sulfonyl) (ammonium salt) (Rhodamine-DMPE). Next, large multilamellar vesicles (LMVs) were formed by hydrating the lipid cakes in 1 mL of 100 mM HEPES buffer (pH 7.4) containing 5 mM $CaCl_2$ and 140 mM NaCl (HEPES buffer hereafter). The suspension of LMVs was incubated in a water bath at 60 °C for 1 h and then sonicated at 60 °C for 30 min upon which the turbid solution became translucent, indicating the formation of SUVs. The solution containing the SUVs was centrifuged for 30 min at 100,000 × *g* and the supernatant (containing the SUVs) was aliquoted and used the same day or immediately frozen in liquid N_2 and stored at −80 °C.

2.6. Proteoliposome Preparation. Proteoliposomes were prepared by placing a 1 mL aliquot of the P2X1-liposomes in a water bath at 35 °C. Next, 24 mM C12E9 in HEPES buffer was added in six 14.4 μL aliquots at 10 min intervals with gentle agitation after each addition. After the final addition of C12E9, 2.5 μL of 166 μg / mL P2X1 in PBS 0.4 mM C12E9 (final concentration ∼ 3 nM P2X1) was added and the SUV protein solution was incubated for 1 h at 35 °C, after which the solution was incubated for another 2 h on a nutating mixer at 4 °C. After incubation, the solution was transferred to a 50 kDa cutoff dialysis cassette (Tube-O-DIALYZER, G-Biosciences, St. Louis, MO, USA) and floated in 800 mL of HEPES buffer with 1 mL of SM2 BioBead slurry (Bio-Rad Laboratories, Hercules, CA, USA) at 4 °C. The buffer was exchanged four times at 4 h intervals. Finally, 5 μL of 1 M trehalose in HEPES buffer was added to the final proteoliposome solution to make the final concentration 5 mM of trehalose. The solution was divided into aliquots, flash-frozen in liquid N_2, and stored at −80 °C until use. For proteoliposomes used for super-resolution imaging, the proteoliposomes were prepared as described earlier, but with the inclusion of 50 nm Envy Green beads (Bangs Laboratories, Inc., Fishers, IN, USA).

2.7. Lipid Bilayer Formation. All membranes were formed on hydrophilically treated borosilicate glass coverslips to facilitate the formation of the lipid bilayer. The coverslips were heated at 80 °C for 30 min in a solution of water, concentrated nitric acid, and 30% hydrogen peroxide (1:1:1 by volume). The coverslips were then rinsed with a copious amount of purified water and dried under a gentle stream of prepurified nitrogen. A single coverslip was then placed into a sample holder and fitted with a Parafilm gasket containing an 8-mm hole cut into its center. For bilayers containing the P2X1 receptor, a 1:1 mixture of protein-free and P2X1-containing proteoliposomes was used. A 50 μL aliquot of the appropriate SUV solution was placed in the center hole of the Parafilm gasket on the hydrophilically treated glass coverslip and incubated at room temperature for 40 min during which the SUVs fused to the glass substrate, ruptured, and formed a continuous bilayer. Bilayers made from DPPC-liposomes were incubated at 45 °C for 2 h (the liquid-to-gel phase transition of DPPC is 41 °C). After incubation, the SUV solution above the bilayer was carefully removed, and the solid supported lipid bilayer membrane was gently rinsed six times with HEPES buffer. For SUVs that contained PEG-PE (at 1.4 mole percent), the PEG-PE formed a cushion between the lipid bilayer and the solid glass support. Cremer and co-workers have shown that this is the optimal condition to minimize protein interactions with the underlying substrate without interfering with protein mobility.[21,22]

2.8. Fluorescence Recovery After Photobleaching. Fluorescence recovery after photobleaching (FRAP) was used to measure the lateral diffusion of labeled lipids in the membrane and to determine the liquid-to-gel phase transition temperature of the P2X1-lipid bilayer. In this experiment, an Olympus IX71 microscope was used and a small well-defined area of fluorescently labeled lipids was photobleached using two-photon excitation from a Spectra-Physics femtosecond Ti:Sapphire laser tuned to 780 nm (Spectra Physics Mai Tai; 100 MHz repetition rate, 80 fs FWHM pulse widths). The two-photon technique has the advantage that the bleached area is very small and bleaching occurs rapidly (limited by the shutter speed, which was 1 ms in this study).[23−25] The FRAP recovery was measured using a Hg:Xe arc lamp that was passed through an optical shutter and a 555 nm bandpass filter (25 nm FWHM; Chroma Technologies Corp), and directed to a 1.4 NA apochromatic 100× microscope objective (Olympus, Inc.) with a dichroic mirror (U-N86016; Chroma Technologies Corp). The laser was passed through a fast optical shutter (model LASSHU_PSFIB; Olympus Inc.) and directed into the microscope objective with a second dichroic mirror (FF749-SDi01; Semrock, Inc.). The laser was attenuated such that the initial bleached area was ∼70% of the original fluorescence intensity and Gaussian in shape (FWHM = 1.2 μm and the average power was ∼30 mW). The fluorescence was collected by the objective, passed through both dichroic mirrors, then through a 605 nm bandpass filter (40 nm FWHM; Chroma Technologies Corp), and imaged onto a Hamamatsu ORCA II CCD camera. The optical shutters were synchronized, and data acquisition was achieved with a custom script written within the Advanced Metamorph software suite (Olympus Inc.). Temperature control was achieved with a custom-made sample cell and objective collar to match and maintain the sample and microscope objective temperature. In this experimental design, two identical PID temperature controllers were utilized (Model SYL-1512A2; Auber Instruments Inc.) and the temperature monitored with matching Pt temperature sensors (Model TH100PT; Thorlabs Inc.). FRAP experiments were performed for temperatures ranging from 10−32 °C. Data analysis was performed using a combination of the Advanced Metamorph software suite (Olympus, Inc.), IGOR Pro (Wavemetrics), and MATLAB (MathWorks Inc.).

To calculate the lateral diffusion coefficients associated with the recovery of the labeled lipids, eq 1 was used.[23]

$$D = \left(\frac{\omega^2}{4t_{1/2}}\right)\gamma_D \tag{1}$$

where ω is the FWHM of the Gaussian profile of the photobleached area generated immediately after its exposure to the FRAP laser, $t_{1/2}$ is the time required for the photobleached

https://dx.doi.org/10.1021/acs.jpcb.0c05474
J. Phys. Chem. B 2020, 124, 7791−7802

spot to recover to $^1/_2$ its maximum value, and γ_D is a correction factor that depends on the bleaching time and the shape of the bleached area. The value of γ_D was 1 for our experiments. Raw "gray scale" data were used to determine the percentage of recoveries. To identify potential phase transitions, the calculated diffusion coefficients were plotted as a function of temperature (Figure 1).

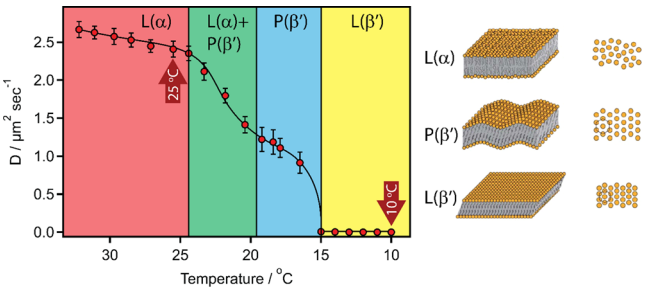

Figure 1. Diffusion coefficients of membrane-incorporated Rhodamine-DMPE as a function of temperature. The different distinct phases are shown on the right side of the graph. The yellow area is the temperature range in which the membrane is in its gel phase L(β'), the blue area is the temperature range in which the membrane is in its ripple P(β') phase, the green area is a mixed-phase region, and the red area is the temperature region in which the membrane exists in its liquid crystalline L(α) phase. The two arrows at 25 and 10 °C indicate the temperature points where ligand binding and super-resolution studies were carried out.

2.9. Optical Setup of the Single-Molecule Microscope. For stochastic kinetic measurements, excitation of the sample was achieved with a stabilized cw-He:Ne laser emitting 633 nm. The beam was first passed through a laser line filter (633/10 X; Chroma Tech.) and then through a $^1/_4$ waveplate (WPQ05M-633; Thorlabs, Inc.) to produce a circularly polarized laser beam. The beam was focused with a 150 mm achromatic lens and directed to the far edge of a 100x 1.45 NA apochromatic TIRF microscope objective (Olympus Inc.) with a dichroic mirror (D-03-R635-t3; Semrock, Inc.) to produce an evanescent field at the interface between the glass coverslip and the lipid bilayer via total internal reflection (TIR; laser power before TIR was 0.94 mW). The fluorescence from individual probe molecules was collected by the microscope objective, passed through the dichroic mirror and a longpass filter (ET655lp; Chroma Tech.), and imaged onto an EMCCD camera (iXon 888; Andor Tech.) with a 300 mm achromatic lens. The exposure time was set to 50 ms, and the frame rate was only slightly higher at 50.02 ms. All stochastic kinetic measurements were performed at 25 °C. Temperature control was maintained at the sample and the microscope objective with a custom-made sample holder and objective collar. The sample holder and the objective collar were both fitted with separate Peltier coolers (TEC3−2.5; Thorlabs Inc.) and interfaced to separate Meerstetter Engineering temperature controllers (model TEC-1091). The temperature was monitored at the sample with a Pt temperature sensor (TH100PT; Thorlabs Inc.) and the hot side of the Peltier coolers with a thermistor (TH10K; Thorlabs Inc.). Single-molecule tracking was performed with an automated tracking algorithm based on the work by Crocker and Grier and programmed into MATLAB (MathWorks Inc.) using modified scripts written by M. Kilfoil and co-workers at the University of Massachusetts Amherst, as well as by the authors.[26,27]

For super-resolution experiments, a cw-He:Ne laser emitting 633 nm and an Nd:YAG laser emitting 532 nm radiation were used as excitation sources. The 633 nm beam was first passed through a laser line filter, followed by a $^1/_4$ waveplate as described earlier, and an electrooptic modulator (Conoptics Model 370 equipped with a Conoptics Model 302 amplifier). The 532 nm beam was first passed through a laser line filter (LL01−532; Semrock, Inc.), a $^1/_4$ waveplate (WPQ05M-532; Thorlabs, Inc.), and then through an electrooptic modulator (Conoptics Model 380C equipped with a Conoptics Model 3 amplifier). After passing through the electrooptic modulators, the beams were aligned to be colinear with each other. The beams were focused with a 150 mm achromatic lens and directed to the far edge of a 100x 1.45 NA apochromatic TIRF microscope objective (Olympus Inc.) with a dichroic mirror (FF545/650-Di01; Semrock, Inc.) to produce an evanescent field at the interface between the glass coverslip and the lipid bilayer (total internal reflection; the laser power before TIR was ∼1 mW). The fluorescence from individual ATP* molecules and Envy Green beads were collected by the microscope objective, passed through a longpass filter (HQ550LP; Chroma) and a notch filter (HSPF-632.8-1.0; Kaiser Optical Systems, Inc.), and imaged onto the EMCCD camera with a 300 mm achromatic lens. All super-resolution imaging experiments were performed at 10 °C. The electro-optic modulators and EMCCD were synchronized through a signal generator (Stanford Research Systems DS345). For data collection, the exposure time was set to 50 ms and the frame rate was 50.02 ms. Super-resolution data sets consisted of 100 movies, each 120 s long, and collected in a single position. Unlike the other single-molecule fluorescence experiments, during the time traces for the super-resolution experiments, the excitation wavelength was alternated between 633 and 532 nm every other frame. This allowed for near-simultaneous tracking of the fiducial marker (Envy Green beads) and the monitoring of ATP* binding to P2X1.

2.10. Measurement of Stochastic Photoblinking and Photobleaching of ATTO-700. The photoblinking and photobleaching properties of ATTO-700 were measured by incorporating ATTO-700-DPPE into the top leaflet of preformed DPPC planar supported membranes (described earlier). Incorporation of ATTO-700-DPPE into the top leaflet of the bilayers ensured that the probe molecules would not interact with the underlying glass support. This was achieved by adding 60 μL of 789 pM ATTO-700-DPPE in HEPES buffer to the top of the membrane followed by incubation at 45 °C for 1 h. After incubation, the solution above the sample was carefully removed and the membrane was rinsed six times with fresh, filtered HEPES buffer. The sample was protected from light at all steps. Next, the sample was affixed to the single-molecule microscope described above and allowed to equilibrate to 25 °C for at least 30 min. This temperature is below the liquid-to-gel phase transition of DPPC ensuring that the ATTO-700 probe molecules remained immobilized throughout the experiments. Each movie was recorded on a part of the sample that had not been exposed previously to the excitation field. A shutter was synchronized to open with the first frame of the movie and remained open until just after the last frame was collected. Each movie lasted at least 100 s to ensure that all ATTO-700 molecules within the field of view were bleached, and a total of 1162 individual probe molecules were recorded at 25 °C.

https://dx.doi.org/10.1021/acs.jpcb.0c05474
J. Phys. Chem. B 2020, 124, 7791−7802

2.11. Measurement of Stochastic Binding of ATTO-700 Labeled ATP to P2X1 Receptors. For kinetic measurements of ATTO-700-labeled ATP (ATP* hereafter) binding to the P2X1 receptor, the buffer above the membrane containing the reconstituted receptors was gently removed and replaced with 60 μL of 100 pM ATP* in HEPES buffer in the dark. The sample was affixed to the single-molecule microscope and equilibrated at 25 °C for at least 30 min prior to data collection. Each experiment lasted for at least 100 s with the laser power and the excitation train being identical to the ATTO-700 bleaching and blinking experiments. A shutter was placed in front of the cw-He:Ne laser and synchronized with the camera as described earlier. Unlike the blinking and bleaching experiments, 10 consecutive movies were recorded in the same area of the membrane to observe repeated ATP* binding to the same individual P2X1 receptors and then repeated at different locations to increase the size of the overall data set.

2.12. Super-Resolution Imaging. For super-resolution imaging, samples were prepared as described earlier, but instead used the proteoliposomes containing Envy Green beads, to serve as fiduciary markers for drift correction. For these experiments, the buffer above the membrane was gently removed and replaced with 60 μL of 500 pM ATP* in HEPES buffer before being introduced to the single-molecule microscope and allowed to equilibrate to 10 °C for 30 min. The sample was excited with 633 nm (red channel) and 532 nm (green channel) laser lines using alternating laser excitation (ALEx). As described earlier, the electrooptic modulators were synchronized with the data collection so the sample was only excited with 633 or 532 nm every other frame, and a shutter in front of the lasers was synchronized to open just prior to collection of the first frame and closed immediately following collection of the last frame of each movie. Super-resolution images of repeated binding events, at each of the three individual P2X1 receptor binding pockets, were reconstructed using point accumulation for imaging in nanoscale topography (PAINT), frame-to-frame drift correction, and fluorescently labeled ATP.

PAINT super-resolution reconstruction was carried out by first cropping the movies around likely P2X1 receptor locations, making sure to include fiducial markers in the frame. After cropping, each diffraction-limited spot (both red and green channels) was fit to a two-dimensional Gaussian to determine its super-localization. The location determined from the red channel was then drift-corrected against the location of the fiduciary markers determined in the green channel of the following frame. Only long tracks of the ATP* (red channel) were considered for the analysis and the subdiffraction-limited localizations collecting into a single image map with contours that define the P2X1 receptor binding pockets.

3. RESULTS AND DISCUSSION

3.1. Phase Characteristics of P2X1 Planar Lipid Bilayers and Super-Resolution Results. Measuring the temperature dependence of the lateral diffusion of fluorescent lipid components within the lipid bilayer using FRAP allowed for the determination of the phase transition temperatures (T_C) and the temperature ranges best suited for ATP binding and PAINT studies.[28] FRAP measurements were therefore conducted within a temperature range of 10−32 °C, and the diffusion coefficients and standard deviations were determined by averaging 10 separate FRAP measurements at each temperature point (eq 1). It is well known that the motion of membrane proteins within a lipid bilayer is greatly affected by its phase.[27,29,30] Figure 1 shows a plot of membrane diffusion coefficients vs temperature and shows that the T_C for the $L(\beta') \rightarrow P(\beta')$ phase transition is 15 °C, the T_C for the $P(\beta') \rightarrow P(\beta') + L(\alpha)$ phase transition is at 19 °C, and the T_C for the $P(\beta') + L(\alpha) \rightarrow L(\alpha)$ phase transition is at 24 °C, where $L(\alpha)$ = liquid crystalline phase, $P(\beta')$ = rippled phase, $L(\beta')$ = gel phase, and $P(\beta') + L(\alpha)$ = mixed phase. Similar reports across a narrower temperature range are consistent with the results we show here.[25]

Below 15 °C, the membrane is essentially frozen and the embedded P2X1 receptor at 10 °C is effectively immobilized, freezing out the slow translational motion and rotational degrees of freedom (Figure 1). This observation allowed the measurement of repeated binding of ATP* to individual static P2X1 receptors and the use of PAINT super-resolution microscopy to construct contour maps of each separate binding site on individual receptors. In Figure 2, the resultant images show triangular clusters of ATP* molecules spaced between 36 and 50 Å apart, similar to the locations of the binding sites identified in crystal structures of P2X receptors (Figure 2F).[1] Our experiments demonstrate that ATP* binds to the ligand-binding pockets of P2X1 receptors, as opposed to being nonspecifically associated with the protein or lipid membrane. Above the $P(\beta') \rightarrow P(\beta') + L(\alpha)$ phase transition, P2X1 receptors pick up rotational degrees of freedom and slowly diffuse. Consequently, it is not possible to generate high-resolution contour plots above 15 °C.

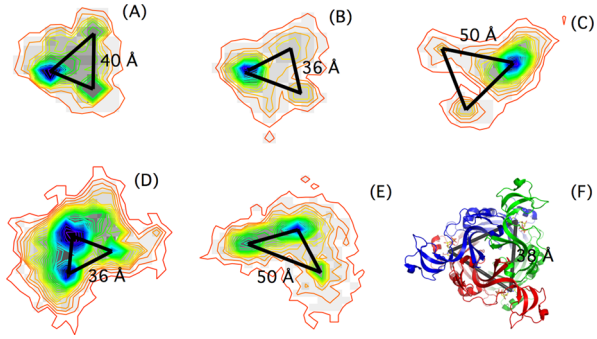

Figure 2. (A−E) Super-resolution contour plots of ATP* molecules binding to individual P2X1 receptors. The super-resolution reconstruction used a 0.25 nm pixel overlaid with contour plots showing three distinct binding sites on individual receptors. (F) Structure of the P2X1 receptor (modeled from the P2X4 crystal structure; PDBID: 4DW1) is drawn to scale for comparison.[1] The triangles indicate the distances between the peaks in the contour plot and correspond to the spatial distance between individual binding sites.

3.2. Rates of Photoblinking and Photobleaching for ATTO-700 at 25 °C. There are complications associated with the utilization of time-lapse fluorescence microscopy to study the binding of ligands to a receptor. In particular, analysis is complicated by the photophysics of the fluorescent probe molecule that is responsible for blinking, which means that the probe molecule can emit light intermittently by reversible entering a dark state such as a long-lived triplet state (or some other dark state). In addition to blinking, a fluorescent molecule will eventually bleach, which is an irreversible chemical change that results in a complete loss of fluorescence.

https://dx.doi.org/10.1021/acs.jpcb.0c05474
J. Phys. Chem. B 2020, 124, 7791−7802

To accurately measure the binding interactions of fluorescently labeled molecules, it is, therefore, necessary to understand these underlying photophysical and photochemical properties of the fluorophore alone. The strategy is to then use the Hidden Markov Models to separate the kinetics associated with blinking and bleaching and to help elucidate hidden processes associated with the allosteric motions in the receptor by incorporating the time the system resides in each state.

To this end, fluorescence blinking and photobleaching rates were measured at 25 °C under the same conditions as those used for ATP* binding, yielding traces that show blinking cycles and eventual bleaching. In Figure 3 it can be seen that as

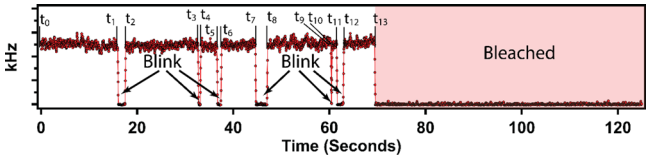

Figure 3. Fluorescence time trace of a single ATTO-700-DPPE molecule embedded in a DPPC lipid bilayer. The data were taken at 25 °C, and the liquid to gel phase transition for DPPC is T_C = 41 °C; the membrane is in its gel phase (frozen).[32,33] This prevents rapid lipid diffusion and allows for ATTO-700-DPPE blinking dynamics to be directly observed until the probe bleaches. The molecule was excited with the 633 nm line of a He:Ne laser that was attenuated to 0.75 mW at the sample (the same as the ligand-binding studies). Fluorescence from single ATTO-700 molecules was collected with a custom single-molecule fluorescence microscope equipped with a 1.45 NA microscope objective and an iXon Ultra 888 EMCCD camera. The excitation laser was synchronized to the start of the data collection by a mechanical shutter with a 1 ms rise time.

the laser is turned on at t_0, ATTO-700 fluoresces; transitioning rapidly between the singlet ground state (gs) and the lowest singlet excited state with a probability of emitting a photon each cycle in accordance with its quantum yield (QY = 0.25 according to the manufacturer). This transition is much faster than the time resolution of the measurement, leading to an observed steady-state fluorescence signal fluctuating around a mean molecular brightness that continues until t_1. At t_1, ATTO-700 enters into a blinking state, presumed to be an excited triplet state, and is nonfluorescent until t_2 when it returns back to the fluorescent state until reaching time t_3; a total of six blink states with seven fluorescent states were observed in this particular time trace. Eventually, at time t_{13}, ATTO-700 enters into a permanent nonemitting state and does not recover back to the fluorescent state (irreversible bleaching). The transitions between states are marked by the fluorescence signal turning off, back on, and permanently turning off. In this way, each state can be unambiguously identified. Based on these observations, a simple phenomenological kinetic model can be used to describe the blinking and bleaching process, a model that is devoid of the underlying photophysical and photochemical rates. This simple kinetic model is given in Figure 4A in which the fluorescing state is connected to a reversible blinking process and an irreversible bleaching process. The experiments yielded 1162 individual recorded events and were analyzed by two different methods.

The first method was to build separate transition probability distributions for blinking, recovery, and bleaching (Figure 4B–D). With this method, the probability distribution for blinking is constructed from observations of single-molecule transitions from the fluorescent (FL) to the blink (B) state. Using Figure 3 as an example, the FL → B transitions are t_1-t_0, t_3-t_2, t_5-t_4, etc. (note t_b-t_a = t_b minus t_a). The transition probability distribution for recovery is then constructed from the observations of single-molecule B → FL transitions (t_2-t_1, t_4-t_3, t_6-t_5 ... in Figure 3), and the transition probability distribution for bleaching is constructed by measuring the entire time individual molecules are in FL before they bleach (FL → b; (t_1-t_0) + (t_3-t_2) + (t_5-t_4) + (t_7-t_6) + (t_9-t_8) + $(t_{11}-t_{10})$ + $(t_{13}-t_{12})$). The bin sizes in the probability distributions are set using the Freedman–Diaconis[31] rule, and the area under the curve is set to one. Since each state can be unambiguously identified according to the phenomenological model, each probability distribution is characterized by a first-order rate equation;

$$p_{FL\to B}(t) = A^* e^{-k_B^{Fit} t} \tag{2}$$

$$p_{B\to FL}(t) = A^* e^{-k_{-B}^{Fit} t} \tag{3}$$

$$p_{FL\to b}(t) = A^* e^{-k_b^{Fit} t} \tag{4}$$

Fits of the probability distributions, using eqs 2–4, reveal exponential distributions for $p_{FL\to B}(t)$, $p_{B\to FL}(t)$, and $p_{FL\to b}(t)$, confirming that the simple phenomenological model (Figure 4A) is valid for ATT-700 under the above-described experimental conditions. The rate constants of this model are 0.082, 0.52, and 0.22 s^{-1} for blinking, recovery, and bleaching, respectively (Figure 4B–D).

The second method of extracting rate constants from single-molecule trajectories used a nonergodic Markov Model (all states were identified, and the bleach state is considered a drain state; also known as an absorbing Markov Chain) and a Baum–Welch maximum likelihood estimator. In this method, the classical rate equations are recast into a probabilistic framework and represented in a matrix formalism (eqs 5–7).

$$\frac{dP(t)}{dt} = P(t)Q \tag{5}$$

$$P(t) = \begin{pmatrix} P_{Fl}(t) \\ P_B(t) \\ P_b(t) \end{pmatrix} \tag{6}$$

$$Q = \begin{pmatrix} -(k_B + k_b) & k_B & k_b \\ k_{-B} & -(k_{-B}) & 0 \\ 0 & 0 & 0 \end{pmatrix} \tag{7}$$

where $\boldsymbol{P}(t)$ is a column vector of the probabilities that the system will be in one of the three states (*Fl*, *B*, or *b*) at some time, t, after the excitation light has been turned on. $\boldsymbol{Q}$ is a matrix of rate constants, and integration gives the Kolmogorov or Master equation (eq 8);

$$P(t) = \begin{pmatrix} P_{Fl}(\Delta t) \\ P_B(\Delta t) \\ P_b(\Delta t) \end{pmatrix} = e^{Qt} E(0) \tag{8}$$

where e^{Qt} is a matrix exponential called the transition probability matrix $\boldsymbol{T}(t)$ that described the probability of making a transition from some starting state to one of the

https://dx.doi.org/10.1021/acs.jpcb.0c05474
J. Phys. Chem. B 2020, 124, 7791–7802

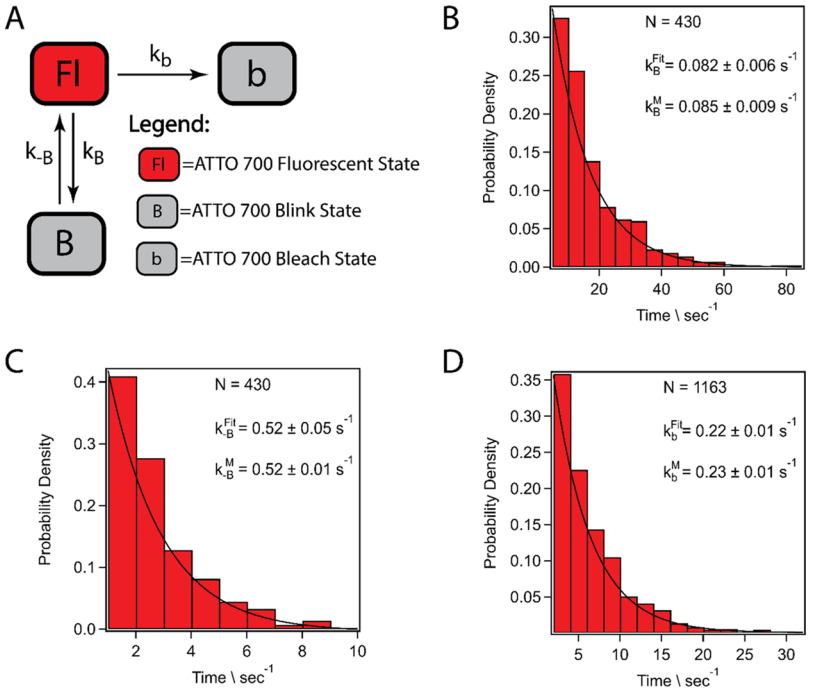

Figure 4. (A) Phenomenological model for blinking and bleaching in ATTO 700; k_B = blinking rate constant, k_{-B} = rate constant for recovery from a blink, and k_b = bleaching rate constant. (B) Probability distribution of the times ATT0−700 is in the fluorescent state (FL) before it undergoes a transition to the blink state. The black line is an exponential fit of the experimental data; N = total number of blinks observed in the data set, k_B^{Fit} = the blinking rate constant determined for the exponential fit (black line), k_B^M = blinking rate constant determined from a Markov analysis using a Baum−Welch maximum likelihood estimator. (C) Probability distribution of the times ATT0−700 is in the blink state before it undergoes a transition back to the fluorescent state. The black line is an exponential fit of the experimental data; N = total number of blinks, k_{-B}^{Fit} = the recovery from a blink rate constant determined for the exponential fit (black line), k_{-B}^M = rate constant determined from a Markov analysis. (D) Probability distribution of the total times ATT0−700 is in the fluorescent state before it bleaches. The black line is an exponential fit of the experimental data; N = total number of times traces in the data set, k_b^{Fit} = bleaching rate constant determined for the exponential fit (black line), k_b^M= bleaching rate constant determined from a Markov analysis.

other two states. Using a discrete time representation gives the discrete transition probabilities for individual steps in the absorbing Markov chain over a discrete time interval $\boldsymbol{\Delta t}$ (50 ms for all experiments carried out in this study):

$$\mathrm{P}(\Delta \mathrm{t}) = \begin{pmatrix} P_{Fl}(\Delta t) \\ P_B(\Delta t) \\ P_b(\Delta t) \end{pmatrix} = \mathrm{T}(\Delta \mathrm{t})\mathrm{E}(0) = e^{\mathrm{Q}\Delta t}\mathrm{E}(0) \tag{9}$$

where

$$\mathrm{T}(\Delta \mathrm{t}) = \begin{pmatrix} 1 - (p_{Fl\to B} + p_{Fl\to b}) & p_{FL\to B} & p_{Fl\to b} \\ p_{B\to Fl} & 1 - (p_{B\to Fl} + p_{B\to b}) & p_{B\to b} \\ 0 & 0 & 1 \end{pmatrix} \tag{10}$$

where p represents the state-to-state transition probabilities for Δt within the transition probability matrix $\boldsymbol{T(\Delta t)}$. $\boldsymbol{E(0)}$ is called the emission matrix or observation matrix. Since each state is a separate observable, $\boldsymbol{E(0)} = \boldsymbol{I}$; an identity matrix. For the HM analysis, we divided the data into three nearly even data sets and used the HM training algorithms available in MathLab (MathWorks, Inc.) to estimate the state-to-state transition probabilities for each. These algorithms implemented a maximum likelihood analysis using the Baum−Welch method. Estimates for the rate constants were then calculated from the matrix logarithm of $\boldsymbol{T(\Delta t)}$;

$$\mathrm{Q} = \frac{1}{\Delta t}\ln[\mathrm{T}(\Delta \mathrm{t})] \tag{11}$$

From the three data sets, the average and standard deviation were calculated. Although the analyses used in this second method are different from those described in the first method earlier, the HM analysis provided identical results to those obtained by fitting the probability distributions (k_B^M, k_B^M, and $k_B^M$are the results of the HM analysis shown in Figure 4). This convergence of results shows that it is possible to accurately and confidently describe the underlying photophysical and photochemical properties of the fluorescent molecules used in this study. Such detailed knowledge of blinking and bleaching has enabled us to account for their variance in all subsequent analyses of ATP* binding to P2X1 receptors.

3.3. Kinetic Rates of ATP* Binding to the P2X1 Receptor. It is believed that conformational flexibility of the membrane may be a necessary condition to fully open the integral ion channel of P2X1 receptors, and for this reason, all ATP* binding experiments were performed at 25 °C.[2,17] Using the custom-built single-molecule fluorescence microscope developed for this task, we were able to directly monitor the binding of ATP* to P2X1 receptors for the first time (Figure 5). A total of 1227 binding events were collected for analysis and represent ∼41 h of recorded data.

Based on X-ray crystallography and mutagenesis, it is known that ATP binds to a cavity between subunits of the P2X1

https://dx.doi.org/10.1021/acs.jpcb.0c05474
J. Phys. Chem. B 2020, 124, 7791−7802

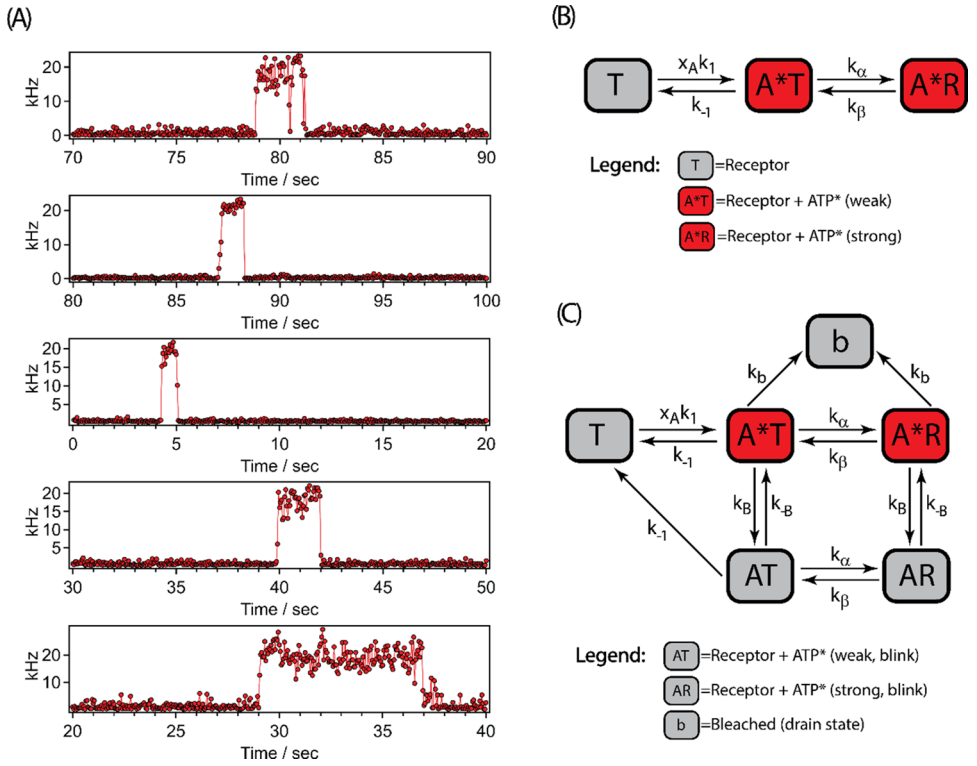

Figure 5. (A) Examples of the single-molecule time traces of ATP* binding to a P2X1 receptor. (B) Phenomenological model of ATP* binding to a P2X1 receptor without taking photophysics into account; k_1 = the forward rate of the unbound state to the weak binding state, x_A = equilibrium concentration of ATP* in solution, k_α = forward rate constant of the weak binding state going to the strong binding state, k_β = rate constant for going from the strong binding state back to the weak binding state, and k_{-1} is the rate constant for ATP dissociating from the weak binding state. (C) Phenomenological model of ATP* binding to the P2X1 receptor, which takes into account the blinking and bleaching of ATTO-700 probe molecule; k_B = blinking rate constant, k_{-B} = rate constant for recovery from a blink, and k_b = bleaching rate constant.

receptor. This binding results in a conformational change in the protein that is thought to cause the tightening of subunits around bound ATP, which induces an allosteric opening of the integral ion channel.[1] Using the results of the single-molecule fluorescence time trajectories (Figure 5A) we can extract the ligand binding rate constants for the mechanism shown in Figure 5B; where $x_A k_1$ is the concentration-dependent forward rate constant for the unoccupied receptor transitioning to a weakly bound state on the P2X1 receptor (x_A = concentration of ATP* in solution), k_α is the forward rate constant for the transition from the weakly bound state to the strongly bound state, k_β is the rate constant for the transition from the strongly bound state going back to the weakly bound state, and k_{-1} is the rate constant for ATP* dissociating from the weakly bound state. Dissociation of ATP from the strong binding state is ignored because structural evidence shows that the two adjacent subunits that create the binding pocket close around a bound ATP, "like a pair of jaws," as stated by Kawate et al., preventing it from dissociation.[1] It is reiterated that these measurements were conducted at equilibrium and the dynamics are obtained from monitoring the fluctuations of ATP* binding and dissociating from a P2X1 receptor. These types of measurements are not possible using methods that yield ensemble averages.

When ATP* binds to the P2X1 receptor, we observe the receptor transition from an unbound, nonfluorescent "dark," state to a bound, fluorescent "bright," state, which becomes dark again when ATP* dissociates. Moreover, even if the ATP* is bound to the P2X1 receptor, it can enter a dark state caused by blinking or bleaching. Our analysis reveals that while there are only two fluorescent states that can be observed (bright and dark), the underlying mechanism contains 6 states connected by 7 rate constants that lead to those observations (Figure 5C). The process is greatly simplified by only considering the transition from bright → dark and fixing the underlying blinking and bleaching rate constants to the values we previously measured for the unbound fluorophore. This reduces our analysis to two observables and three unknown rate constants with transition probabilities for this process is given by:

$$\mathrm{P}(\Delta t) = \begin{pmatrix} P_{\mathrm{A^*T}}(\Delta t) \\ P_{\mathrm{A^*R}}(\Delta t) \\ P_{\mathrm{AT}}(\Delta t) \\ P_{\mathrm{AR}}(\Delta t) \\ P_{\mathrm{T}}(\Delta t) \\ P_{b}(\Delta t) \end{pmatrix} = e^{\mathrm{Q}\Delta t}\mathrm{E}(0) \tag{12}$$

where the rate constant matrix is given by eq 12,

https://dx.doi.org/10.1021/acs.jpcb.0c05474
J. Phys. Chem. B 2020, 124, 7791−7802

$$Q = \begin{pmatrix} -(k_\alpha + k_B + k_{-1} + k_b) & k_\alpha & k_B & 0 & k_{-1} & k_b \\ k_\beta & -(k_\beta + k_B + k_b) & 0 & k_B & 0 & k_b \\ k_{-B} & 0 & -(k_{-B} + k_\alpha + k_{-1}) & k_\alpha & k_{-1} & 0 \\ 0 & k_{-B} & k_\beta & -(k_{-B} + k_\beta) & 0 & 0 \\ 0 & 0 & 0 & 0 & 0 & 0 \\ 0 & 0 & 0 & 0 & 0 & 0 \end{pmatrix} \quad (13)$$

and the emission matrix is given by eq 14.

$$E(0) = \begin{pmatrix} 1 & 0 \\ 1 & 0 \\ 0 & 1 \\ 0 & 1 \\ 0 & 1 \\ 0 & 1 \end{pmatrix} \quad (14)$$

The emission matrix has two columns, with column 1 denoting underlying states that lead to the bright observation and column 2 denoting the states that lead to a dark observation. For the HM analysis, the data are divided into 3 equal data sets and analyzed with the HM training algorithms available in MathLab (MathWorks, Inc.) as we described for the properties of the unbound fluorophore. The difference is that the Baum−Welch maximum likelihood algorithm is modified to hold the transition probabilities for blinking and bleaching constant while allowing T, A*T, and A*R to reach their most likely values. This allows estimates for the rate constants to be calculated from the matrix logarithm of the transition probability matrix obtained from the HM analysis (eq 11) as follows:

$$T(\Delta t) = \begin{pmatrix} p_{A^*T} & p_{A^*T\to A^*R} & p_{A^*T\to AT} & p_{A^*T\to AR} & p_{A^*T\to T} & p_{A^*T\to b} \\ p_{A^*R\to A^*T} & p_{A^*R} & p_{A^*R\to AT} & p_{A^*R\to AR} & p_{A^*R\to T} & p_{A^*R\to b} \\ p_{AT\to A^*T} & p_{AT\to A^*R} & p_{AT} & p_{AT\to AR} & p_{AT\to T} & p_{AT\to b} \\ p_{AR\to A^*T} & p_{AR\to A^*R} & p_{AR\to AT} & p_{AR} & p_{AR\to T} & p_{AR\to b} \\ 0 & 0 & 0 & 0 & 1 & 0 \\ 0 & 0 & 0 & 0 & 0 & 1 \end{pmatrix} \quad (15)$$

$$p_{A^*T} = 1 - (p_{A^*T\to A^*R} + p_{A^*T\to AT} + p_{A^*T\to AR} + p_{A^*T\to T} + p_{A^*T\to b}) \quad (16)$$

$$p_{A^*R} = 1 - (p_{A^*R\to A^*T} + p_{A^*R\to AT} + p_{A^*R\to AR} + p_{A^*R\to T} + p_{A^*R\to b}) \quad (17)$$

$$p_{AT} = 1 - (p_{AT\to A^*T} + p_{AT\to A^*R} + p_{AT\to AR} + p_{AT\to T} + p_{AT\to b}) \quad (18)$$

$$p_{AR} = 1 - (p_{AR\to A^*T} + p_{AR\to A^*R} + p_{AR\to AT} + p_{AR\to T} + p_{AR\to b}) \quad (19)$$

where;

$$p_{A^*T\to AR} \cong p_{A^*R\to AT} \cong p_{A^*R\to T} \cong p_{A^*R\to b} \cong p_{AT\to A^*R} \cong p_{AT\to b} \cong p_{AR\to A^*T} \cong p_{AR\to T} \cong p_{AR\to b} \cong 0 \quad (20)$$

The results of this HM analysis allows us to report for the first time, the rates of transition between strong and weak binding states of a ligand−receptor interaction, as well as the elementary rate for a ligand dissociating from its initially formed weak binding state (Table 1, Figure 5C). From the rate data gathered in this study and the value of k_1 obtained from our earlier study (k_1 = 1.142 × 10^6 M^{-1} sec^{-1}), the microequilibrium constants, as well as the overall dissociation constant, were determined from: $K_{\alpha/\beta} = k_\alpha/k_\beta$, $K_{1/-1} = k_1/k_{-1}$, and $K_d = \frac{1}{K_{1/-1}\times K_{\alpha/\beta}}$ (Table 1). The results show that a change in free energy due to the allosteric motion of the P2X1 receptor tightening around ATP is $\Delta G(25°C) = -RT\ln(K_{\alpha/\beta}) = -3.7$ kJ mol^{-1}. This is about 1.5 times greater than $N_A k_B T$ which is a significant thermodynamic driving force favoring the strongly bound state, but low enough that the process is reversible at 25 °C as expected. For completeness, the analysis was also carried out by including a dissociation pathway from the strong binding state. The analysis gave a near-zero rate constant for A*R → T ($k_{A^*R\to T}$ = 5.6 × 10^{-5} sec^{-1}) and left all other rate constants unchanged. This gives additional evidence supporting the framework model shown in Figure 5.

Table 1. Rate Constants, Microequilibrium Constants, and the Overall Equilibrium Constant for the Binding and Unbinding of ATP* to the P2X1 Receptor as Shown in Figure 5[a]

rate constants		equilibrium constants	
k_{-1}	0.51 ± 0.06 s^{-1}	[b]$K_{1/-1}$	2.24 × 10^6 M^{-1}
k_α	1.41 ± 0.04 s^{-1}	$K_{\alpha/\beta}$	4.41
k_β	0.32 ± 0.01 s^{-1}	K_d	102 nM

[a]The constants were derived from the HM analysis described in section 3.3. $K_{\alpha/\beta} = k_\alpha/k_\beta$, $K_{1/-1} = k_1/k_{-1}$, and $K_d = \frac{1}{K_{1/-1}\times K_{\alpha/\beta}}$. [b]$k_1$ = 1.142 × 10^6 M^{-1} s^{-1} from Ruepp et al.[20]

Finally, we can validate these results by comparing the overall dissociation constant determined in our study ($K_d^{\text{single molecule}}$ = 102 nM) with the value from previous bulk measurements; K_d^{Bulk} = 119 nM.[20] This unequivocally shows that the results presented here are in agreement with these earlier affinity measurements and provide support for the measured rate constants and microequilibrium constants determined through single-molecule observation.

3.4. Significance of Blinking and Bleaching in the HM Analysis. A fundamental question arising from this study is whether blinking and bleaching affect the measured biophysical

https://dx.doi.org/10.1021/acs.jpcb.0c05474
J. Phys. Chem. B 2020, 124, 7791−7802

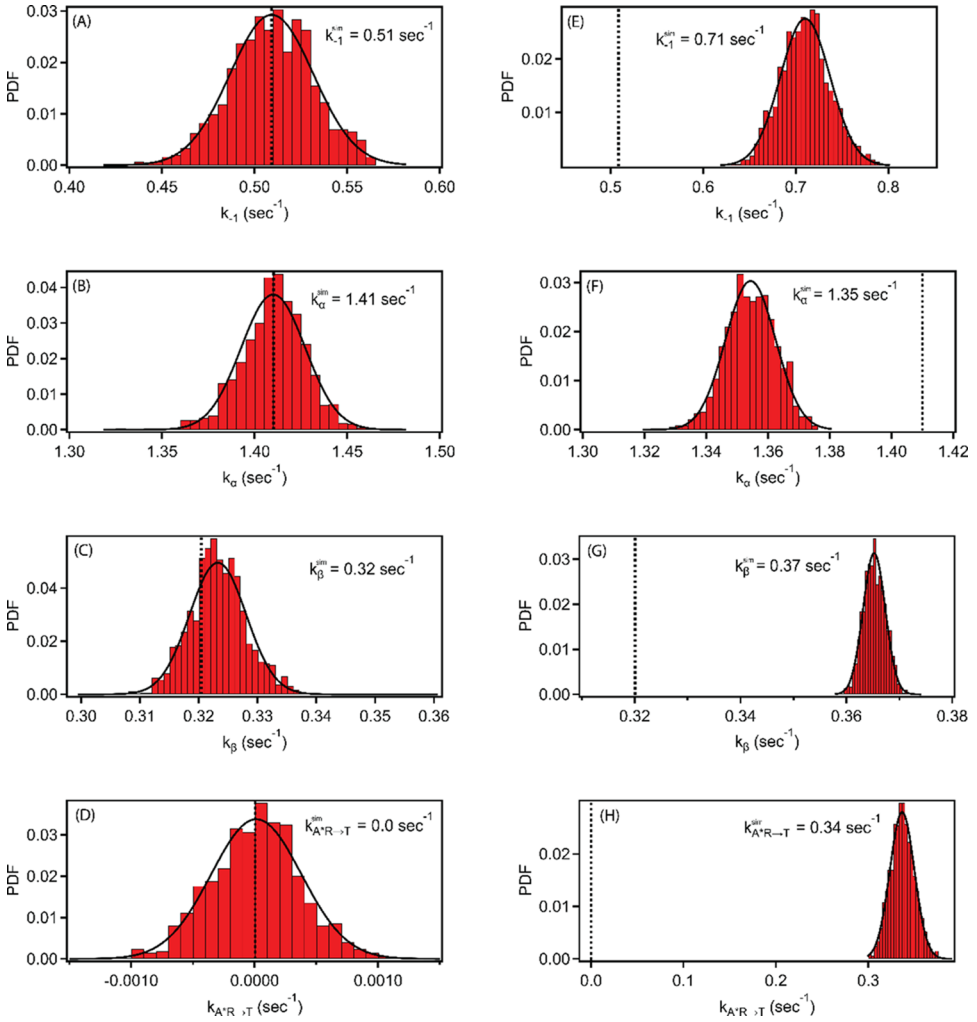

Figure 6. Results from stochastic simulations and HM analysis. The red bars are probability distributions of the rate constants extracted using an HM analysis, the dotted lines are the values entered into the simulations, and the black lines are fits to a Gaussian PDF. (A-D) Results from the HM maximum likelihood analysis that includes blinking and bleaching rates. (E-H) Results from the HM maximum likelihood analysis that ignores blinking and bleaching rates. $x_A k_1$ was set to zero, and T was treated as a drain state in these simulations.

rate constants extracted by the HM analysis. To address this question, we carried out a series of simulations based on the mechanism shown in Figure 5C. The base simulations generated 1227 nonergodic Hidden Markov walks where the starting state is A*T, the drain states are T and b ($x_A k_1$ is set to zero), and the time interval between steps is set to 50 ms. T, AT, AR, and b are all assigned as dark states, A*T and A*R are assigned as bright states, and the rate constants are set to the values measured from the experimental data sets. Like the experimental data, the simulated time traces are divided into three equal data sets and analyzed in one of two ways. The first was to perform the HM analysis in the same manner as described earlier, by constraining the blinking and bleaching rate constants of the ATP-attached ATTO-700 dye. The second was to analyze the time traces using the three-state model shown in Figure 5B which ignores the blinking and bleaching rates. This entire process was then repeated 1000 times. The resultant rate constants extracted from the HM analysis are displayed as histograms using the Freedman−Diaconis rule, normalized such that the area under the curve is 1 and fitted to a Gaussian probability density function (PDF). The results in Figure 6 show the outcome, with the red bars representing the rate constants extracted from the simulations using the HM analysis (k_{-1}^{sim}, k_{α}^{sim}, k_{β}^{sim}, $k_{A\times R\rightarrow T}^{sim}$), the black lines represent the Gaussian fit, and the dotted vertical lines are the experimental values that were used to generate the simulations. In panels 6A−D, we see the HM analysis that includes the blinking and bleaching rates (k_B, k_{-B}, and k_b). The rate constants for k_{-1}^{sim}, k_{α}^{sim}, k_{β}^{sim}, and $k_{A^*R\rightarrow T}^{sim}$ all agree well with the values used to carry out the simulations, thus providing confidence in the HM analysis to extract experimental values. Even when different initial values were provided as inputs to the HM analysis, convergence to the same rate constant was always achieved, proving the MLA method to be a robust analytical approach. As such, we can be confident that dissociation from a tight binding state is highly unlikely as an analysis that ignores the dynamics originating from ATTO-700 has a nonzero A*R→T dissociation rate, and the resultant increase in the A*T→T rate results in an overall dissociation constant (K_d = 622 nM) that is far from the value measured in bulk experiments.[20] In contrast, the values for k_{-1}^{sim}, k_{α}^{sim}, k_{β}^{sim}, and $k_{A^*R\rightarrow T}^{sim}$ do not agree with the simulation input parameters when blinking and bleaching are ignored, thus supporting the importance of including these rates in the analysis.

https://dx.doi.org/10.1021/acs.jpcb.0c05474
J. Phys. Chem. B 2020, 124, 7791−7802

4. CONCLUSIONS

Here, we presented the first description of single-molecule interactions between ligand-gated ion channels and their native ligand. We achieved this by analyzing 1227 independent binding events with high temporal resolution (50 ms) and through a super-resolution imaging study. The super-resolution PAINT experiments at 10 °C clearly demonstrate that repeated ATP* binding is highly specific, and contour-maps distinguish three distinct orthosteric binding sites on each P2X1 receptor at locations that coincide with binding sites seen in X-ray crystallography.[1] Single-molecule fluorescence studies of lipid-bound ATTO-700 allowed the rate constants for blinking and bleaching to be measured and were critical for the subsequent correction of ATP* binding kinetics. The inclusion of these constants was also shown to be critical in our stochastic simulations that were used to validate the constrained HM analysis.

By knowing that ATP* binds to the native ligand binding sites and by measuring the intrinsic dynamics of ATTO-700, it was possible to measure the kinetic rate constants for an ATP* molecule transiting across multiple binding states: from a weak binding state to a strong binding state (k_α = 1.41 sec^{-1}), from the strong binding state to the weak binding state (k_β = 0.32 sec^{-1}), and dissociation from the weak binding state (k_{-1} = 0.51 sec^{-1}). Direct measurement of such state transitions has not been previously reported. Using the measured rate constants, we estimated the overall K_d = 102 nM and found it was satisfactory compared to the bulk measurements made elsewhere.[20] Here, we were also able to determine the free energy resulting from the allosteric motions of the P2X1 receptors as the orthosteric site contracts around ATP* and found the value to be −3.7 kJ mol^{-1} which is 1.5 times greater than $N_A k_B T$ which is a significant thermodynamic driving force favoring the strongly bound state, but low enough that the process is reversible at 25 °C

The methods described here provide a straight forward approach for understanding molecular-scale interactions, such as the engagement of target proteins by small molecules or antibodies. Rate constants were simply calculated by measuring the dwell times of ATP* on the P2X1 receptor, and if coupled with single-channel electrophysiological measurements, would enable a direct and complete molecular description of all the state transitions associated with the process of ligand binding and gating. Importantly, the methods presented here are widely applicable to all membrane proteins and provide a new means of monitoring ligand interactions across a class of therapeutic targets that have traditionally been hard to address.

AUTHOR INFORMATION

Corresponding Author

J. A. Brozik − *Department of Chemistry, Washington State University, Pullman, Washington 99164-4630, United States;* orcid.org/0000-0003-2097-5051; Email: brozik@wsu.edu

Authors

K.-T. Lam − *Department of Chemistry, Washington State University, Pullman, Washington 99164-4630, United States*

E. L. Taylor − *Department of Chemistry, Washington State University, Pullman, Washington 99164-4630, United States;* orcid.org/0000-0002-6460-1871

A. J. Thompson − *Department of Pharmacology, University of Cambridge, Cambridge CB2 1TN, United Kingdom*

M.-D. Ruepp − *UK Dementia Research Institute at King's College London, London WC2R 2LS, U.K.; Institute of Biochemistry and Molecular Medicine, University of Bern, 3012 Bern, Switzerland*

M. Lochner − *Institute of Biochemistry and Molecular Medicine, University of Bern, 3012 Bern, Switzerland;* orcid.org/0000-0003-4930-1886

Michael J. Martinez − *Department of Chemistry, Washington State University, Pullman, Washington 99164-4630, United States*

Complete contact information is available at: https://pubs.acs.org/10.1021/acs.jpcb.0c05474

Notes

The authors declare no competing financial interest.

ACKNOWLEDGMENTS

This work was supported by the Air Force Office of Scientific Research FA9550-18-1-0344 (J.A.B.)

REFERENCES

(1) Kawate, T.; Michel, J. C.; Birdsong, W. T.; Gouaux, E. Crystal structure of the ATP-gated P2X4 ion channel in the closed state. *Nature* **2009**, *460*, 592−598.

(2) Mansoor, S. E.; Lü, W.; Oosterheert, W.; Shekhar, M.; Tajkhorshid, E.; Gouaux, E. X-ray structures define human P2X3 receptor gating cycle and antagonist action. *Nature* **2016**, *538*, 66−71.

(3) Dionne, V. E.; Leibowitz, M. D. Acetylcholine receptor kinetics. A description from single-channel currents at snake neuromuscular junctions. *Biophys. J.* **1982**, *39*, 253−261.

(4) Riedel, T.; Lozinsky, I.; Schmalzing, G.; Markwardt, F. Kinetics of P2X7 Receptor-Operated Single Channels Currents. *Biophys. J.* **2007**, *92*, 2377−2391.

(5) Jahr, C. E.; Stevens, C. F. Voltage dependence of NMDA-activated macroscopic conductances predicted by single-channel kinetics. *The Journal of Neuroscience* **1990**, *10*, 3178−3182.

(6) Shi, J.; Dertouzos, J.; Gafni, A.; Steel, D., Chapter 7 Application of Single-Molecule Spectroscopy in Studying Enzyme Kinetics and Mechanism. *In Methods in Enzymology*, Academic Press: 2008; *450*, 129−157.

(7) Weiss, S. Fluorescence Spectroscopy of Single Biomolecules. *Science* **1999**, *283*, 1676−1683.

(8) Nie, S.; Chiu, D. T.; Zare, R. N. Probing individual molecules with confocal fluorescence microscopy. *Science* **1994**, *266*, 1018−1021.

(9) Nie, S.; Zare, R. N. Optical Detection of Single Molecules. *Annu. Rev. Biophys. Biomol. Struct.* **1997**, *26*, 567−596.

(10) McQuarrie, D. A. Stochastic Approach to Chemical Kinetics. *J. Appl. Probab.* **1967**, *4*, 413−478.

(11) Colquhoun, D.; Hawkes, A. G.; Katz, B. Relaxation and fluctuations of membrane currents that flow through drug-operated channels. *P. Roy. Soc. B-Biol. Sci.* **1977**, *199*, 231−262.

(12) Qin, F.; Auerbach, A.; Sachs, F. Maximum likelihood estimation of aggregated Markov processes. *P. Roy. Soc. B-Biol. Sci* **1997**, *264*, 375−383.

(13) Milescu, L. S.; Akk, G.; Sachs, F. Maximum likelihood estimation of ion channel kinetics from macroscopic currents. *Biophys. J.* **2005**, *88*, 2494−2515.

(14) Milescu, L. S.; Yildiz, A.; Selvin, P. R.; Sachs, F. Maximum likelihood estimation of molecular motor kinetics from staircase dwell-time sequences. *Biophys. J.* **2006**, *91*, 1156−1168.

(15) Müllner, F. E.; Syed, S.; Selvin, P. R.; Sigworth, F. J. Improved hidden Markov models for molecular motors, part 1: basic theory. *Biophys. J.* **2010**, *99*, 3684−3695.

(16) Syed, S.; Müllner, F. E.; Selvin, P. R.; Sigworth, F. J. Improved hidden Markov models for molecular motors, part 2: extensions and application to experimental data. *Biophys. J.* **2010**, *99*, 3696−3703.
(17) Barnaba, C.; Martinez, M. J.; Taylor, E.; Barden, A. O.; Brozik, J. A. Single Protein Tracking Reveals that NADPH Mediates the Insertion of Cytochrome P450-Reductase into a Biomimetic of the Endoplasmic Reticulum. *J. Am. Chem. Soc.* **2017**, *139*, 5420−5430.
(18) Barden, A. O.; Goler, A. S.; Humphreys, S. C.; Tabatabaei, S.; Lochner, M.; Ruepp, M.-D.; Jack, T.; Simonin, J.; Thompson, A. J.; Jones, J. P.; Brozik, J. A. Tracking individual membrane proteins and their biochemistry: The power of direct observation. *Neuropharmacology* **2015**, *98*, 22−30.
(19) Rollins, G. C.; Shin, J. Y.; Bustamante, C.; Pressé, S. Stochastic approach to the molecular counting problem in superresolution microscopy. *P Natl Acad Sci.* **2015**, *112*, E110−E118.
(20) Ruepp, M.-D.; Brozik, J. A.; de Esch, I. J. P.; Farndale, R. W.; Murrell-Lagnado, R. D.; Thompson, A. J. A fluorescent approach for identifying P2X1 ligands. *Neuropharmacology* **2015**, *98*, 13−21.
(21) Wiznerowicz, M.; Trono, D. Conditional Suppression of Cellular Genes: Lentivirus Vector-Mediated Drug-Inducible RNA Interference. *J. Virol.* **2003**, *77*, 8957−8951.
(22) Privé, G. G. Detergents for the stabilization and crystallization of membrane proteins. *Methods* **2007**, *41*, 388−397.
(23) Kubitscheck, U.; TschodrichRotter, M.; Wedekind, P.; Peters, R. Two-photon scanning microphotolysis for three-dimensional data storage and biological transport measurements. *J Microsc-Oxford* **1996**, *182*, 225−233.
(24) Albertorio, F.; Diaz, A. J.; Yang, T.; Chapa, V. A.; Kataoka, S.; Castellana, E. T.; Cremer, P. S. Fluid and air-stable lipopolymer membranes for biosensor applications. *Langmuir* **2005**, *21*, 7476−7482.
(25) Poudel, K. R.; Keller, D. J.; Brozik, J. A. The effect of a phase transition on single molecule tracks of Annexin V in cushioned DMPC assemblies. *Soft Matter* **2012**, *8*, 11285−11293.
(26) Axelrod, D.; Koppel, D.; Schlessinger, J.; Elson, E.; Webb, W. Mobility measurement by analysis of fluorescence photobleaching recovery kinetics. *Biophys. J.* **1976**, *16*, 1055.
(27) Poudel, K. R.; Keller, D. J.; Brozik, J. A. Single particle tracking reveals corralling of a transmembrane protein in a double-cushioned lipid bilayer assembly. *Langmuir* **2011**, *27*, 320−327.
(28) Tamm, L. K.; McConnell, H. M. Supported phospholipid bilayers. *Biophys. J.* **1985**, *47*, 105−113.
(29) Crocker, J. C.; Grier, D. G. Methods of digital video microscopy for colloidal studies. *J. Colloid Interface Sci.* **1996**, *179*, 298−310.
(30) Gillespie, D. T. Exact Stochastic Simulation of Coupled Chemical Reactions. *J Phys. Chem* **1977**, *81*, 2340.
(31) Freedman, D.; Diaconis, P., On the histogram as a density estimator: L 2 theory. *Probability theory and related fields* Springer 1981, *57* (4), 453−476.
(32) Almeida, P. F. F.; Vaz, W. L. C.; Thompson, T. E. Lateral diffusion in the liquid phases of dimyristoylphosphatidylcholine/cholesterol lipid bilayers: a free volume analysis. *Biochemistry* **1992**, *31*, 6739−6747.
(33) Filippov, A.; Orädd, G.; Lindblom, G. Lipid Lateral Diffusion in Ordered and Disordered Phases in Raft Mixtures. *Biophys. J.* **2004**, *86*, 891−896.

https://dx.doi.org/10.1021/acs.jpcb.0c05474
J. Phys. Chem. B 2020, 124, 7791−7802